THE ASTROPHYSICAL JOURNAL, 519:244–256, 1999 July 1

VLBA OBSERVATIONS OF 12 GHz METHANOL MASERS TOWARD W3(OH)

L. MOSCADELLI[1] AND K. M. MENTEN
Max-Planck-Institut für Radioastronomie, Auf dem Hügel 69, 5300 Bonn 1, Germany
C. M. WALMSLEY
Osservatorio Astrofisico di Arcetri, Largo E. Fermi 5, 50125 Firenze, Italy
AND
M. J. REID
Harvard-Smithsonian Center for Astrophysics, 60 Garden Street, Cambridge, MA 02138, USA
Received 1998 November 28; accepted 1999 February 3

ABSTRACT

We have conducted VLBA observations of the 12 GHz CH_3OH masers toward the ultracompact H II region W3(OH). The angular resolution of ≈ 1 mas is sufficient to resolve most of the maser spots and determine their sizes and brightness temperatures. The FWHM sizes of the spots are found from ≤ 2 to 10 AU with brightness temperatures between 10^9 and 6×10^{11} K. The actual brightness temperatures may be higher (by a factor ≤ 10) than the measured values, because most of the spots have spectral profiles unresolved with our velocity resolution (0.28 km s^{-1}). Our data also suggest the presence of a spatially extended component of maser emission with size ≥ 20 mas and brightness temperature $\leq 10^9$ K.

The comparison of our data with previous 6.7 GHz VLBI observations shows that there is a good spatial (≤ 10 mas) and velocity (within 0.3 km s^{-1}) correspondence between numerous 12 and 6.7 GHz CH_3OH spots. Comparing our maps with those of Menten et al. yields relative proper motions of a few km s^{-1} in magnitude. A "linear structure" of approximately 200 AU in size (P.A. = 141°) is found in the northern methanol maser clump, which also shows a regular trend of radial velocities with projected positions (a velocity gradient of 2400 km s^{-1} pc^{-1}).

Subject headings: H II regions — ISM: individual (W3) — ISM: molecules — masers — radio lines: ISM — stars: formation

1. INTRODUCTION

W3(OH) is probably the most studied ultracompact H II (UC H II) region in our Galaxy owing to its proximity (2.2 kpc; Humphreys 1978) and its powerful maser emission. Radio continuum (Dreher & Welch 1981; Scott 1981) and infrared (Campbell et al. 1989) observations indicate that the central ionizing star is of spectral type O9–O7 with a mass of $\approx 30\ M_\odot$. The high intensity of the continuum and line (atomic and molecular) emission makes interferometric and VLBI (very long baseline interferometry) observations feasible, which allows the study of the environment around a massive star at size scales from 1 to 1000 AU.

Emission of several maser lines of OH and CH_3OH have been observed toward W3(OH). Particularly strong are the 12 GHz $2_0 \rightarrow 3_{-1}$ E and the 6.7 GHz $5_1 \rightarrow 6_0$ A^+ transitions of CH_3OH and the 1665 MHz $^2\pi_{3/2}$ $J = \frac{3}{2}$ $F = 1 \rightarrow 1$ transition of OH. In 1988, a three-station VLBI observation by Menten et al. (1988b) at 12 GHz identified two clusters (size ≈ 100 AU) of maser spots; the richer of these was located toward the northwest border of the UC H II region, and the second cluster was 1".2 south, in the southwest portion of the H II region. The angular resolution of that observation allowed upper limits for the size of single masers spots of 2–3 mas to be determined corresponding to lower limits for the brightness temperature between 2×10^{10} and 4×10^{11} K. A follow-up 6.7 GHz VLBI observation (Menten et al. 1992) showed that, at a comparable flux detection threshold, the 6.7 GHz maser spots are distributed over a more extended area than the 12 GHz masers and that the typical intensity ratio between the 6.7 and the 12 GHz spots is higher than 10. Interestingly, they found that there is a very good correspondence in the relative positions and radial velocities of the most intense maser spots of the two CH_3OH transitions. One expects this to put stringent constraints on models of the maser excitation.

Bloemhof, Reid, & Moran (1992) have measured the proper motions of the 1665 MHz OH maser spots toward W3(OH). The OH spots are spread over the western half of the H II region, where the density of the molecular cloud, based on the observations of thermal lines, may be considerably higher. The observed pattern of OH proper motions suggests expansion from a point within the UC H II region with an expansion velocity of a few km s^{-1}. This has been interpreted as being due to a cometary bow shock induced by the central O star moving at a velocity of several km s^{-1} relative to the surrounding molecular cloud.

However, the kinematics of the ionized and molecular gas around a massive star is still poorly understood. One characteristic peculiar to the 12 GHz and 6.7 GHz CH_3OH masers toward UC H II regions is that the spots are often distributed along lines or arcs of sizes of order of 1"–2" with, occasionally, a monotonic variation of radial velocity along these structures (Norris et al. 1988, 1993, 1998). This is thus an indication that methanol masers trace an ordered motion, whose nature (rotating disk/torus, expanding jet, filaments, etc.) needs clarification.

In order to determine the physical parameters of the 12 GHz maser emission toward W3(OH) better and to study the variability/kinematics of the maser spots, we have reob-

[1] Stazione Astronomica di Cagliari, Loc. Poggio dei Pini, Str. 54, 09012 Capoterra (CA), Italy.

served W3(OH) at 12 GHz using the VLBA. In § 2 of this paper, our observational procedures are described, and in § 3, our maps of the maser emission are presented. In § 4, we compare the properties of the 6.7 and 12 GHz CH_3OH masers, while in § 5, the evidence for proper motions of the maser spots is considered. In § 6, we present our conclusions.

2. OBSERVATIONS AND DATA REDUCTION

W3(OH) was observed using the VLBA[2] on 1994 February 14 and 15, with 34 scans of 6 minutes distributed over 15 hr. Before and after each scan on W3(OH), continuum sources were observed for purpose of calibration. Table 1 reports the coordinates of the sources observed.

The receiver system temperatures T_{sys} were about 60 K for six antennas (Brewster, Fort Davis, Kitt Peak, Owens Valley, Pie Town, and St. Croix), 100 K for Hancock, Mauna Kea, and North Liberty, and 180 K for Los Alamos. The gain factors for the 10 VLBA antennas at 12 GHz range from 0.10 to 0.13 K Jy^{-1}.

Both circular polarizations were recorded with an observing bandwidth of 2 MHz centered at the LSR velocity of -44.0 km s^{-1} (based upon a rest frequency of 12.178595 GHz). Data were correlated at the VLBA correlator (NRAO, Socorro) with 256 spectral points corresponding to a channel separation of 0.19 km s^{-1}. On-line Hanning weighting was applied to individual telescope spectra prior to cross-correlation, so that the postcorrelation velocity resolution is 0.28 km s^{-1}.

The calibration of the visibilities was accomplished with the AIPS package, following the standard procedure for line-VLBI data described by Reid et al. (1980). A single scan of a strong continuum source (NRAO 530) was used to derive the instrumental (time-independent) single-band delay and the phase offset between the two polarizations. After removing the instrumental errors, all calibrator scans were fringe-fitted to determine the residual (time-dependent) delay and the fringe rate. The corrections derived from calibrators were applied to the reference maser feature, and then its data were fringe-fitted to determine the residual fringe rate owing to the inaccuracy in the source position used by the correlator. The phase reference feature (at -45.2 km s^{-1}) was the same as that of Menten et al. (1988b), whose structure consists of two bright spots separated by 4 mas. The visibilities of the reference maser feature were self-calibrated (five "phase-only" and two "phase and amplitude" iterations) to remove atmospheric fluctuations. Next, the visibility phases of all other velocity channels were corrected by subtracting the phase of the reference feature. Total power spectra were used to derive the bandpass response of each antenna and to derive the gains needed to calibrate in amplitude the visibilities.

TABLE 1

OBSERVED SOURCES

Sources	α (1950)	δ (1950)	Type[a]
W3(OH)	02 23 16.400	61 38 57.00	M
3C 84	03 16 29.569	41 19 51.94	C
NRAO 150	03 55 45.256	50 49 20.29	C
OJ 287	08 51 57.253	20 17 58.44	C
4C 39.25	09 23 55.316	39 15 23.51	C
3C 273	12 26 33.248	02 19 43.29	C
3C 279	12 53 35.838	−05 31 08.04	C
3C 345	16 41 17.608	39 54 10.82	C
NRAO 530	17 30 13.534	−13 02 45.78	C
J1800+7828 (1803+784)	18 03 39.179	78 27 54.30	C
J1924−2914 (1921−293)	19 21 42.238	−29 20 26.42	C
J2007+4029 (2005+403)	20 05 59.560	40 21 01.80	C
BL Lac	22 00 39.363	42 02 08.57	C
3C 454.3	22 51 29.521	15 52 54.31	C

NOTE.—Units of right ascension are hours, minutes, and seconds, and units of declination are degrees, arcminutes, and arcseconds.

[a] M = maser; C = calibrator.

[2] The VLBA is a facility of the NRAO, which is operated by Associated Universities, Inc., under contract with the NSF.

Using the AIPS task IMAGR, we produced for all the emission channels 1.″6 × 3.″3 ($\Delta\alpha \times \Delta\delta$) maps centered 0.″5 south of the reference feature, roughly midway between the northern and southern 12 GHz maser spot clusters found by Menten et al. (1988b). For the purpose of detecting weak maser spots, first naturally weighted maps were produced. Before mapping, the data were Hanning weighted and alternate channels selected. For the naturally weighted maps, the pixel size was 0.4 mas in each coordinate and the restoring (CLEAN) beam was an elliptical Gaussian with 2.1 × 1.6 mas FWHM. The rms noise level on the channel maps, σ, calculated using an area in which no signal is found, is comparable to the expected thermal noise level of 8 mJy $beam^{-1}$ for all the channels in which no intense features ($\leq$10 Jy) are present. If strong emission is found, the rms noise level increases from the thermal value up to 200 mJy $beam^{-1}$ scaling with maximum intensity.

Every channel map was searched for emission above a certain threshold using the AIPS task SAD, which performs a fit of the detected emission features with single or multiple Gaussians, determining position, flux, and FWHM of the spots. The threshold used was the minimum of the map (taken positive), which is found to vary between channels within the range 0.04–2 Jy $beam^{-1}$. Adopting this threshold, the dynamic range of our maps can be conservatively defined by the ratio of the peak to the absolute value of the minimum, and it ranges between 10 and 130, scaling with the peak intensity of the channel. A feature was considered real if it was found in at least two contiguous channels with a position offset less than the FWHM of the fitted Gaussian profile. The FWHM in velocity of the 12 GHz maser emission for the narrowest lines may be appreciably lower than 0.5 km s^{-1}, our velocity resolution after postcorrelation Hanning smoothing. In order to recover the narrower lines, for any peak found by SAD in only one channel, the contiguous channels were examined for weak features at the same position. If a peak was found with intensity greater than 5 σ and offset less than the FWHM of the Gaussian profile, the component was also considered real. To determine more precise parameters of each feature, the elliptical Gaussian fit was repeated using the AIPS task SJFIT, which employs only a small area (less than 40 × 40 pixels) around the peak. In most cases a single Gaussian fits well the emission profile; however, in three cases, the components are so close that we used a two-component Gaussian fit.

After determining which features were real, in order to study their spatial profiles at higher angular resolution, uniform weighted maps were produced for all the (postcorrelation Hanning smoothed) channels. The restoring (CLEAN) beam is an elliptical Gaussian with 1.1 × 0.7 mas FWHM, and the pixel size is 0.2 mas. For all the

detected maser spots, the AIPS task SJFIT was used again to perform the elliptical Gaussian fit.

In order to compare our results with those of Menten et al. (1988b, 1992), our maps have been restored using the same circular 9.8 mas beam. Then the position of each spatial feature has been determined following the procedure already described. In this case, because of the lower angular resolution, several spots that appeared separated by a few mas in the high angular resolution map, are seen now as a single feature.

3. OBSERVATIONAL RESULTS

In Figure 1, a high-resolution single-dish spectrum of W3(OH), the total power flux density of our observations, and the flux density recovered from the synthesized maps are compared. The comparison between the total power spectra shows well that, at our velocity resolution, the spectral features are smoothed and reduced in intensity. Regarding the flux from the synthesized maps, on average, considering the most intense channels, $\approx 25\%$ of the total power flux density is missed. Our method of calibrating the visibilities using total power spectra should allow agreement within 10%. It is possible that decorrelation effects, which affect the cross–power spectra but not the total power spectra, cause a reduction of the synthesized flux relative to the total flux. However, we doubt this for two reasons. First, we can exclude appreciable reductions of flux density due to errors in the source position used by the correlator. By studying the residual fringe rate of the reference maser feature, an uncertainty $\leq 1''$ is found, which, even on the longest baselines, implies a reduction of the visibility amplitudes of only 2%–3%, too small to explain the missing flux. Second, Menten et al. (1992) measured an even larger amount ($\approx 50\%$) of missing flux for the 6.7 GHz CH_3OH masers toward W3(OH). Since the 12.2 and 6.7 GHz maser emissions are very well correlated, the explanation must be something other than correlator errors, given the different processors used in the two sets of observations (VLBA vs. VLBI MkII).

Another possibility is that the missing flux is associated with undetected maser features, whose intensity is below the detection threshold. Figure 2 presents the histograms of the number of detected spots and the corresponding summed flux versus the single spot flux, taken in bins of 5 Jy. Making an "educated guess" at the number of sources in the first bin, probably 10–100 weak sources are missed, whose summed flux should be of order (or less than) 100 Jy. This would explain only about one-tenth of the missing flux, which, summing over all channels, amounts to ≈ 900 Jy. A larger effect might result from the fact that structures on angular scales larger than our shortest baseline (≈ 200 km) are resolved out. Then their typical size has to be > 20 mas, and correspondingly, in order to match the flux missing on average per channel (≈ 100 Jy), their brightness temperature has to be lower than 3×10^9 K.

Figure 3 compares the distribution of the 12 GHz maser spots with the positions of the 6.7 and 23.1 GHz methanol masers and the 2 cm wavelength continuum emission from the UC H II region. Following the discussion in Menten et al. (1992), the absolute position of the 12 GHz reference spot

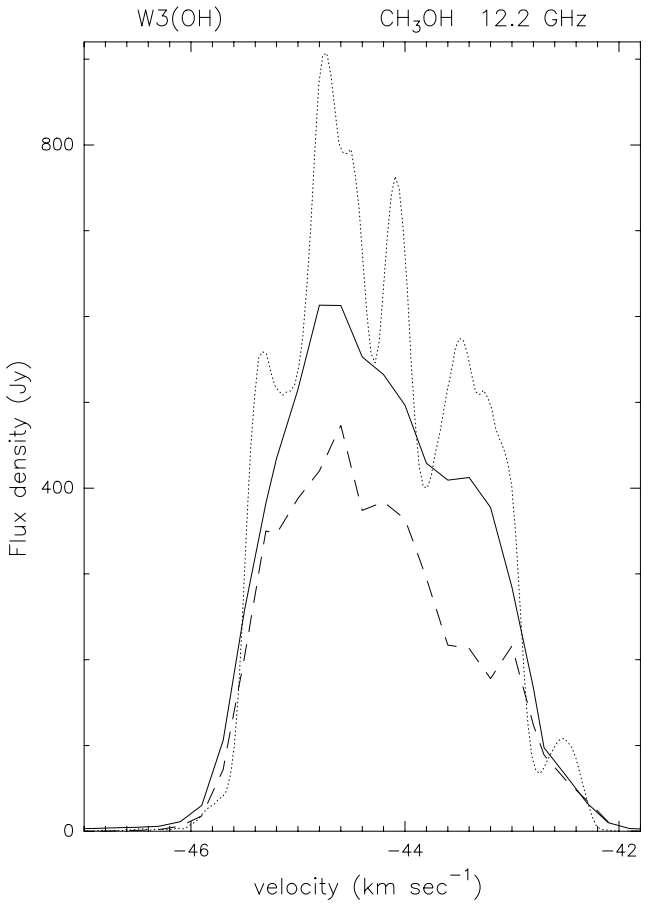

FIG. 1.—High-resolution (0.04 km s^{-1}) single-dish spectrum of W3(OH) (*dotted line*) is compared with the total power spectrum of our observations (*continuous line*) and the integrated flux density of the synthesized maps (*dashed line*), plotted using all the 0.2 km s^{-1} channels.

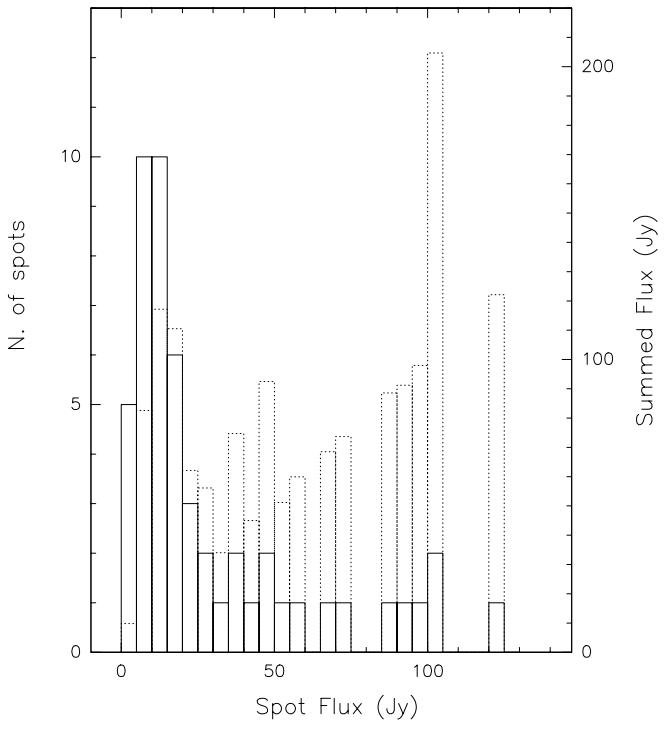

FIG. 2.—Histograms of the "number of detected spots" (*continuous line*) and the "summed flux of detected spots" (*dotted line*) vs. the "spot flux" are compared. The spot flux density is taken in bins of 5 Jy. The left vertical axis gives the number of detected spots, and the right one, the summed flux.

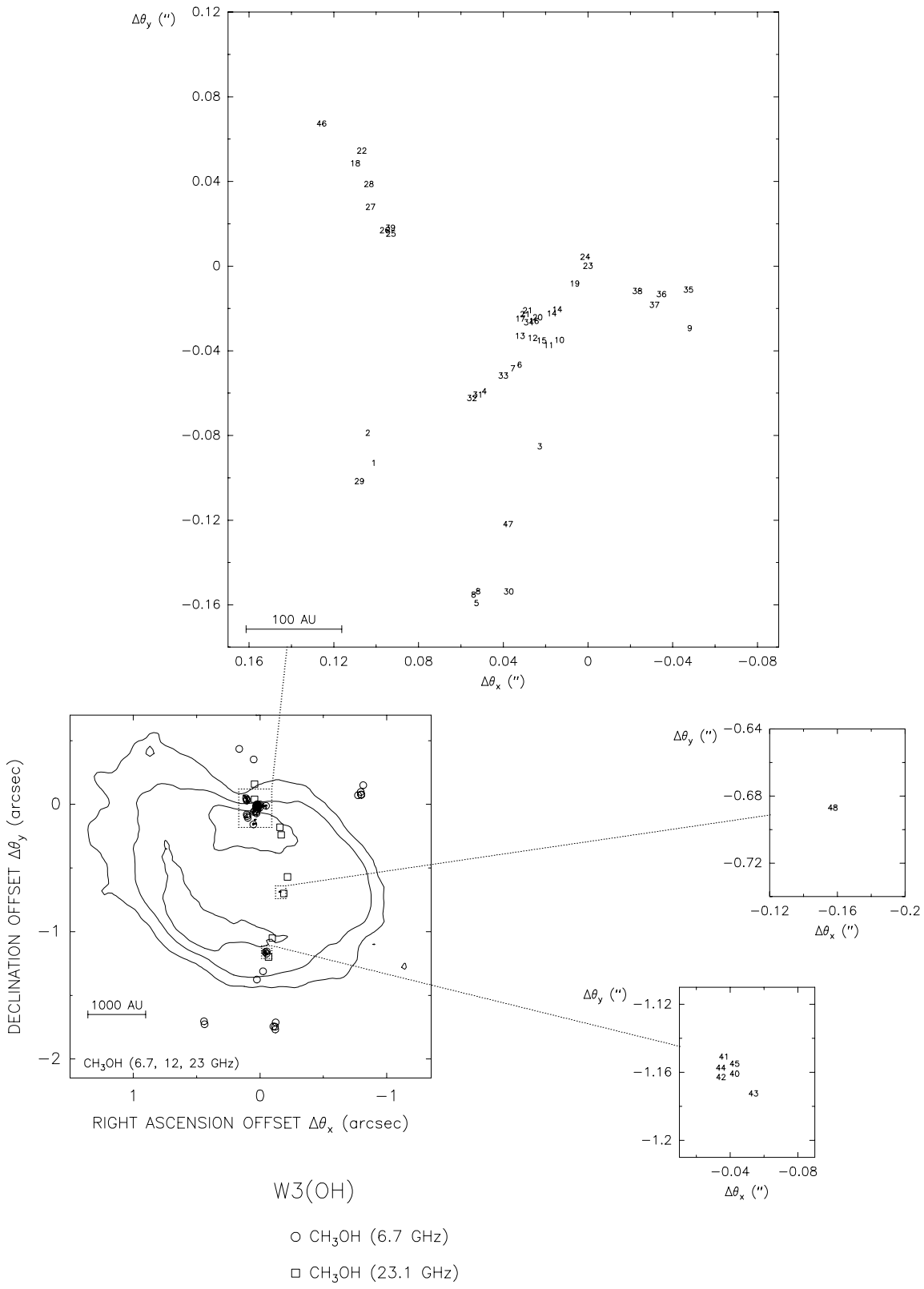

FIG. 3.—Lower left-hand panel shows a comparison of the positions of the 12 GHz CH_3OH masers (this paper) with the distributions of 6.7 GHz (Menten et al. 1992) and 23.1 GHz (Menten et al. 1988a) CH_3OH masers, and the continuum emission at 2 cm. The contour lines represent the 0.5, 7.1, and 16.6 mJy beam^{-1} levels of a VLA 2 cm continuum map (Kawamura & Masson 1998). The 6.7 GHz and 23.1 GHz methanol maser positions are indicated with open circles and open rectangles, respectively. The reference features at 6.7 GHz and 12 GHz are assumed to coincide, and we used the absolute 6.7 GHz position derived by Menten et al. (1992), $(\alpha, \delta)_{J2000} = 2^h27^m03^s.83, +61°52'25''.2$. We also assumed that the brightest spot of the northern clump of the 23.1 GHz CH_3OH maser emission is aligned with the reference spot at 6.7 GHz. The upper panel and the two lower right-hand panels show the detailed distribution of the 12 GHz CH_3OH maser spots, labeled with their component numbers (see Table 2). The upper panel refers to the northern clump, the upper right-hand panel shows the single spot found at the center of the UCH II region, and the lower right-hand panel refers to the southern clump.

is assumed to be the same as that of the reference spot at 6.7 GHz, $(\alpha, \delta)_{J2000} = 2^h27^m03^s.83, +61°52'25''.2$. We have also assumed that the position of the brightest spot of the northern clump of the 23.1 GHz methanol masers (Menten et al. 1988a) coincides with the reference spot at 6.7 GHz. This assumption requires a shift of the VLA positions measured by Menten et al. (1988a) of $\approx 0''.4$ (4 times the reported uncertainty of $0''.1$) and is justified by the fact that the central and southern clumps of the 23.1 GHz emission then coincide with the observed 12 GHz maser clumps. The blowups of the three regions in which maser emission is found show the detailed distributions of the 12 GHz maser spots. Each spot is identified by a number from 1 to 48 corresponding to its entry in Table 2, where the spot parameters are given. All the coordinates are referred to equinox J2000.0. The position uncertainties have been calculated using the relation $\Delta\theta = 0.5 \times \mathrm{FWHM/SNR}$, where FWHM is the full width at half-maximum of the fitted Gaussian and SNR is the ratio between the amplitude and the rms of the Gaussian fit. The relative position accuracy varies from 1 μas to 1 mas, depending on the size and intensity of the spot. The fluxes are measured in the naturally weighted maps (the fluxes of the uniform weighted maps are slightly reduced owing to the lower weighting of the shorter baselines). The other parameters are derived from fits to the uniform weighted maps, taking advantage of the better angular resolution (by a factor of 2).

We identify 48 12 GHz CH_3OH maser spots; 41 are found in the northern clump and six in the southern clump. In both of these clumps, 12 GHz maser emission was detected by Menten et al. (1988b). A single spot is found at an intermediate position between the northern and southern clump, which was not seen by Menten et al. (1988b). For this feature, the formal SNR ratio of the Gaussian fit is high (40), and the measured intensity (2 Jy beam^{-1} in the naturally weighted map) is well above (17 times) the rms noise level of the channel map. However, the flux is compatible with its nondetection in the previous less sensitive observations. This single spot shows that 12 GHz CH_3OH maser emission also emerges from the inner part of the arclike distribution already observed in the 6.7 GHz and 23.1 GHz CH_3 OH masers toward W3(OH).

Figures 4 and 5 present the contour plots of the maser emission for different channels. Figure 4 shows the most intense features of the northern clump, and Figure 5, the emission of the southern clump. The structure of the maser emission appears more complicated than simply a distribution of distinct spots. Toward the southern clump, for

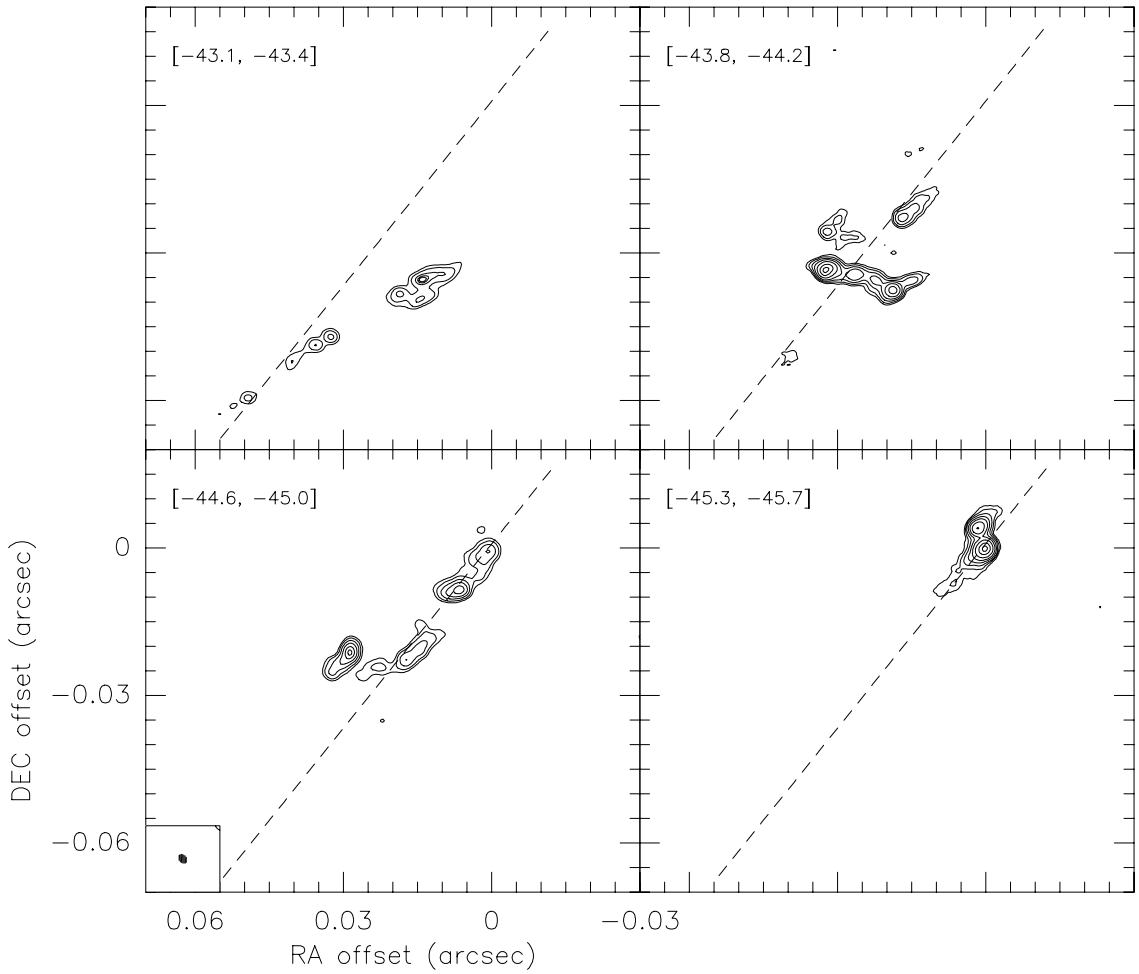

FIG. 4.—Velocity channel contour plots of the 12 GHz CH_3OH emission for the most intense features in the northern clump. Each plot is the average of the two velocity channels (0.5 km s^{-1} velocity resolution) indicated between brackets on the upper left-hand corner of the plot. The levels of brightness temperature used in each contour plot are (1) *upper left-hand*: 0.4, 0.8, 1.6, 2.1, 2.3 $\times$ 10^{10} K; (2) *upper right-hand*: 0.4, 0.8, 1.6, 3.1, 6.2, 12, 18 $\times$ 10^{10} K; (3) *lower left-hand*: 0.7, 1.4, 2.9, 5.8, 12, 17 $\times$ 10^{10} K; (4) *lower right-hand*: 0.2, 0.4, 0.8, 1.6, 2.9, 5.9, 12, 18 $\times$ 10^{10} K. The dashed line represents the axis relative to which the square mean of spot distances is minimum. The naturally weighted beam is shown at the lower left-hand corner of the lower left-hand plot.

TABLE 2

SPOT PARAMETERS[a]

COMPONENT[b]	V_{LSR} (km s^{-1})	Flux[c] (Jy)	T_{br}[d] ($\times 10^{10}$ K)	$\Delta\alpha$[d] (mas)	$\Delta\delta$[d] (mas)	DECONVOLVED Major Axis[d] (AU)	DECONVOLVED Minor Axis[d] (AU)	DECONVOLVED Position Angle[d] (deg)
2	−42.3	14	2.0	103.942(0.089)	−78.878(0.178)	9.0	3.3	18
1	−42.7	34	14	101.146(0.005)	−93.132(0.008)	3.5	1.8	167
3	−43.0	12	2.7	22.790(0.068)	−85.356(0.085)	5.0	3.5	27
4	−43.0	9.0	2.9	48.996(0.059)	−59.312(0.043)	4.1	2.0	104
5	−43.0	22	5.1	52.658(0.059)	−159.334(0.039)	5.5	2.6	99
8a	−43.4	10	1.8	51.892(0.130)	−153.754(0.094)	6.3	3.7	75
8b	−43.4	11	1.8	54.050(0.150)	−155.328(0.116)	8.5	2.9	57
6	−43.4	9.0	4.1	32.318(0.035)	−46.760(0.039)	2.8	2.2	124
7	−43.4	10	3.9	35.486(0.038)	−48.398(0.033)	3.3	1.1	113
11	−43.8	104	42	18.556(0.002)	−37.492(0.002)	3.7	1.8	117
10	−43.4	45	7.4	13.548(0.025)	−35.036(0.016)	6.8	2.2	115
9	−43.8	5.7	3.1	−48.064(0.053)	−29.438(0.065)	0.0	0.0	0
13	−44.2	138	42	32.136(0.004)	−33.096(0.004)	4.8	2.2	127
12	−44.2	68	11	26.160(0.017)	−34.060(0.009)	6.6	2.9	97
15	−4.2	59	11	21.928(0.025)	−35.320(0.021)	5.0	3.1	62
14a	−44.6	100	11	14.562(0.024)	−20.612(0.025)	10	2.9	136
14b	−44.6	47	16	17.158(0.010)	−22.532(0.014)	3.7	2.2	156
17	−44.6	51	11	31.954(0.013)	−25.016(0.013)	4.4	2.4	129
21b	−44.6	122	21	29.684(0.018)	−22.796(0.019)	12	1.3	136
21a	−44.6	73	49	28.478(0.002)	−21.068(0.004)	3.9	0.7	166
16	−44.6	16	3.7	25.524(0.106)	−26.060(0.097)	5.2	4.0	114
18	−44.2	14	2.0	109.906(0.138)	48.422(0.251)	7.0	3.7	179
22	−44.6	20	2.2	106.808(0.147)	54.378(0.326)	11	4.4	167
19	−44.6	98	32	6.258(0.004)	−8.418(0.003)	5.0	1.3	115
20	−44.6	28	2.5	23.770(0.320)	−24.314(0.125)	13	4.4	97
23	−45.3	224	56	0.000	0.000	5.2	3.1	138
24	−45.3	91	37	1.344(0.002)	4.236(0.003)	4.1	1.5	135
26	−45.0	9.5	2.4	96.014(0.092)	16.828(0.134)	5.9	3.5	21
25	−45.0	9.5	2.6	93.054(0.175)	15.182(0.142)	3.3	1.8	79
27	−45.7	8.5	3.4	102.710(0.045)	27.820(0.050)	2.8	2.2	119
28	−46.5	1.3	0.9	103.458(0.111)	38.610(0.258)	3.5	0.7	13
29	−42.3	1.8	1.3	107.930(0.077)	−101.746(0.126)	0.0	0.0	0
30	−42.7	3.1	0.2	37.426(4.940)	−153.846(4.748)	10	9.2	115
31	−43.0	8.0	1.6	52.056(0.138)	−60.834(0.105)	4.4	1.1	116
32	−43.0	8.4	0.8	54.782(0.420)	−62.494(0.347)	6.1	4.2	110
33	−43.4	11	2.7	39.990(0.106)	−51.902(0.134)	7.4	1.3	142
34	−44.2	20	2.1	27.962(0.267)	−26.722(0.142)	9.0	2.4	111
35	−44.2	10	1.2	−47.420(0.575)	−11.300(0.372)	12	4.0	119
36	−44.6	11	4.7	−34.718(0.066)	−13.412(0.069)	2.8	2.0	119
37	−44.6	10	1.1	−31.358(0.404)	−18.420(0.312)	3.7	2.0	81
38	−45.3	0.9	1.4	−23.310(0.482)	−11.958(0.493)	0.0	0.0	0
39	−45.7	2.6	0.2	93.284(0.505)	18.000(0.493)	11	3.5	46
40	−43.0	88	8.0	−42.622(0.049)	−1161.004(0.052)	9.9	4.6	137
45	−43.0	35	2.9	−42.658(0.074)	−1155.094(0.117)	9.2	5.9	178
41	−43.4	18	11	−36.380(0.005)	−1150.902(0.013)	4.1	0.9	175
44	−43.4	39	5.6	−34.550(0.016)	−1157.466(0.092)	14	1.3	174
42	−43.4	16	3.2	−34.614(0.037)	−1162.930(0.105)	6.8	1.8	7
46	−43.0	6.7	0.6	125.786(0.599)	67.200(1.184)	12	5.1	162
43	−43.8	27	3.2	−53.800(0.052)	−1172.588(0.059)	5.9	4.4	142
47	−43.4	7.7	0.5	37.770(1.261)	−122.072(0.688)	6.8	2.9	88
48	−44.2	18	0.7	−157.380(0.047)	−687.184(0.105)	18	6.2	167

[a] Observing date is 1994 Feb 14 and 15.

[b] If future authors need to refer to the single maser spot, the suggested way is " W3(OH):MMWR nn, " where nn indicates the component number.

[c] Fluxes are measured in the naturally weighted maps, whose beam is an elliptical Gaussian with 2.1 × 1.6 mas FWHM.

[d] Brightness temperature, position offsets and sizes are derived from fits to the uniform weighted maps, whose beam is an elliptical Gaussian with 1.1 × 0.7 mas FWHM. For the weak components 39 and 48, these parameters are derived from fits to the naturally weighted maps.

example, several spots are seen connected by a layer of lower intensity emission, and we suspect that dynamic range limitations prevent us seeing similar continuous patterns in the case of the northern clump. The fact that both our maps show evidence for extended structure and that flux is missed relative to the total power spectra, suggests that an extended area of maser emission ($\geq$20 mas) may be present.

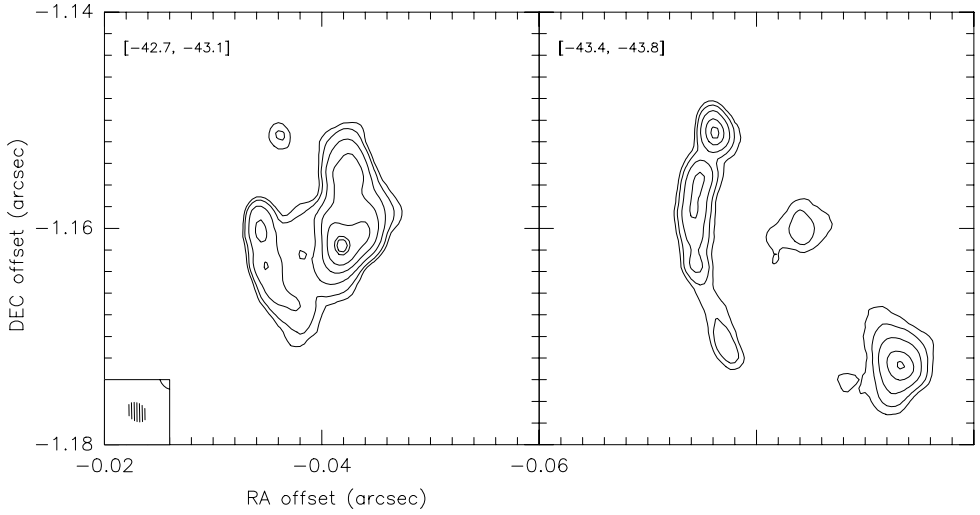

FIG. 5.—Velocity channel contour plots of the 12 GHz CH_3OH emission for the southern clump. Each plot is the average of the two velocity channels (0.5 km s^{-1} velocity resolution) indicated between brackets on the upper left-hand corner of the plot. The levels of brightness temperature used in each contour plot are (1) *left-hand*: 1.5, 2.4, 4.9, 9.8, 20, 39, 44 × 10^9 K; (2) *right-hand*: 1.9, 3.6, 7.2, 14, 22 × 10^9 K. The naturally weighted beam is shown at the lower left-hand corner of the left-hand plot.

Figure 4 shows that the most intense features in the northern clump are distributed mainly along a southeast northwest axis, along which there is a gradient in intensity, with the weakest spots to the southeast extreme and the strongest to the northwest. The position angle (P.A.), east of north, of this axis (plotted in Fig. 4 as a dashed line) is 141°, with a rms scatter of spot positions relative to the axis of 5 mas. Along this axis it is observed a monotonic variation of the radial velocities, which become more redshifted to the southeast. For all the spots of the northern clump, Figure 6 presents the plot of radial velocities versus angular distances projected along an axis at P.A. 141°. The radial velocities of the most intense spots (corresponding to the area plotted in Fig. 4) vary linearly with the projected angular distance. This group of spots seems to be part of a structure characterized by a gradient of radial velocity (V_r)

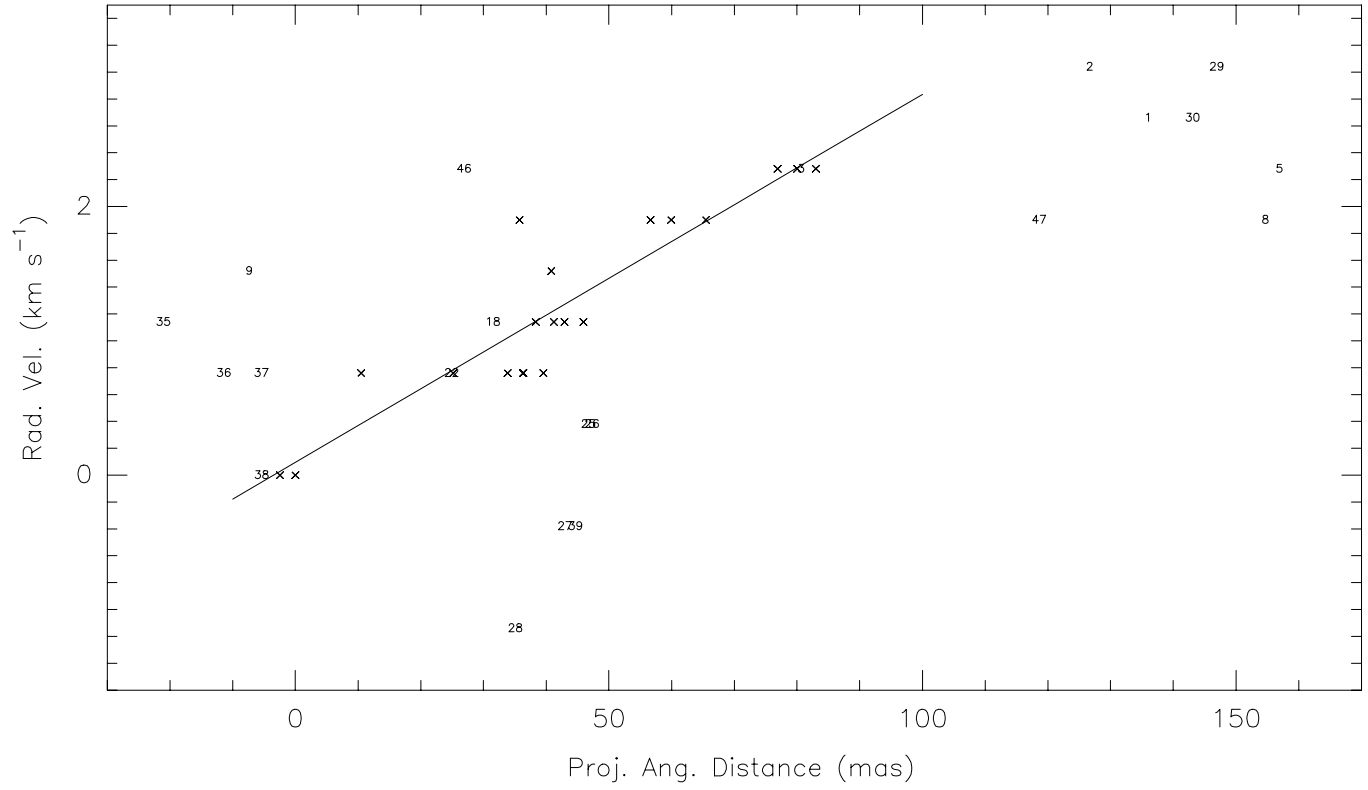

FIG. 6.—For all the spots of the northern clump, the radial velocities are plotted vs. the angular distances projected along an axis at P.A. 141°. Both radial velocities and projected distances are measured respect to the reference spot. The most intense spots along the strip at P.A. 141°, corresponding to the area plotted in Fig. 4, are indicated by crosses. The solid line gives the linear fit of the radial velocities vs. projected distances when only this set of spots is considered. The rest of the spots are indicated with their component numbers (see Fig. 3).

to projected distance (D) of $\Delta V_r/\Delta D = 0.012 \pm 0.002$ km s^{-1} AU^{-1} (2.4×10^3 km s^{-1} pc^{-1}). The size of this apparent structure is roughly 180 AU, which is similar to some of the structures discussed by Norris et al. (1993, 1998). However, spots not aligned with the axis at P.A. 141° or with projected angular distance from the reference spot ≥ 90 mas, do not seem to be associated with this motion.

4. PROPERTIES OF THE 6.7 GHz AND 12 GHz CH_3OH MASERS

Based on Figure 3, one notes that all the detected maser spots at 12 GHz emerge from the region in which the continuum emission at 15 GHz (Kawamura & Masson 1998) is still appreciable (>1 mJy beam^{-1}). The continuum at 15 GHz is delimited by a sharp edge at which the intensity decreases by a factor of 30 across an angular size of $\approx 0\farcs25$. Figure 3 also shows that maser spots at 6.7 GHz are seen beyond the edge of the continuum at 15 GHz. We have compared the 6.7 GHz positions with the map at 8.4 GHz of Wilner, Reid, & Menten (1999), whose beam is $0\farcs2$. The arclike distributions of the 6.7 GHz spots extends in declination over $2\farcs2$, significantly more than the 8.4 GHz continuum in the same range of right ascension ($2''$), and hence it is likely that some 6 GHz spots are outside the lowest contour level (30 μJy beam^{-1}) of the continuum map. That suggests a background free-free intensity at 6.7 GHz for those spots ≤ 30 K. This is in contrast with the high values ($\geq 10^4$ K) used to explain the strong 6.7 GHz CH_3OH maser emission toward W3(OH) in the model of Sobolev, Cragg, & Godfrey (1997).

Table 2 shows that at least half of the spots have deconvolved sizes appreciably larger than the uniformly weighted beam, and, thus, our angular resolution is sufficient to resolve them. This is also shown by the fact that the spot intensity, in Jy beam^{-1}, decreases appreciably (by a factor 2–3) going from the naturally to the uniformly weighted maps. Thus, we are able for the first time to determine the effective sizes of most of the spots and, consequently, their brightness temperatures. As discussed later, our coarse velocity resolution is not sufficient to resolve the spectral profiles of most of the spots. Therefore, the derived brightness temperatures have to be considered as lower limits. Our observations do, however, allow an upper limit to be set to the brightness temperature. Using the high-resolution single-dish spectrum of W3(OH) shown in Figure 1, we calculate upper limits to the mean brightness temperature at any velocity, which are within a factor of 10 of the measured lower limits.

Figure 7 presents the histograms of the spot sizes (defined as the geometrical mean of the major and minor axes) and brightness temperatures. The median spot size is 4 AU consistent with the upper limit of 5–6 AU found by Menten et al. (1988b) for some of the brightest features at 12 GHz. Most of the spots are strongly elongated (the average ratio "major to minor" axis is 3:1), and often contiguous spots are oriented in the same direction, which may be the mark of some underlying structure. Of the 48 spots plotted, two-thirds have brightness temperatures in the range 10^9–10^{11} K, with the most intense spot reaching 6×10^{11} K. The model for the excitation of the 12 GHz CH_3OH masers by Sobolev & Deguchi (1994) can explain brightness temperatures as high as 10^{11} K as being due to pumping by an intense FIR (25–50 μm) radiation field, caused by hot (175 K) dust grains and incident upon a maser clump in the foreground (0.03 pc) relative to the H II region. Our results show that a maser spot in W3(OH) has a median brightness temperature of order 3×10^{10} K, which, according to the Sobolev and Deguchi model, would imply a methanol column density of 6×10^{15} cm^{-2} (here it is assumed a line width, ΔV, of 0.3 km s^{-1}; see below).

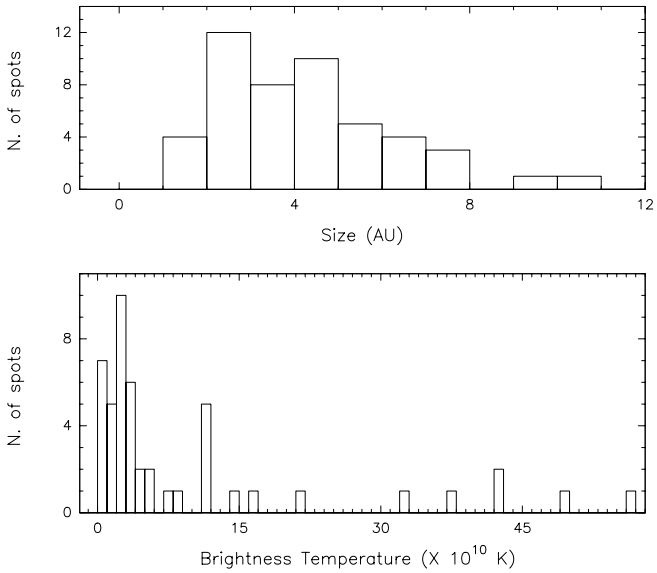

FIG. 7.—Upper plot is the histogram of the spot sizes, defined as the geometrical mean of the major and minor axes (see Table 2). The histogram bin size is 1 AU. The lower plot is the histogram of the brightness temperatures, using a bin size of 10^{10} K. In neither plots do we include the three spots that in Table 2 have a deconvolved size equal to "0," which indicates that they are still unresolved at our angular resolution.

Figure 8 compares the positions of the 6.7 GHz (Menten et al. 1992) and 12 GHz maser spots in the northern and southern clumps. The beam of the synthesized maps of Menten et al. (1992) at 6.7 GHz is 9.8 mas, not sufficient to separate the different centers of maser emission and determine their structure. The spot positions at 6.7 GHz should be regarded as the centroids of emission of (possibly) several "real" spots inside the 10 mas beam. In order to compare our 12 GHz observations with the 6.7 GHz data, the 12 GHz maps were restored using the same beam as at 6.7 GHz and the parameters of the spots as seen with this resolution determined (see Fig. 10 and Table 3 for more details). Comparing the 1988 12 GHz data with the 1992 6.7 GHz results, and assuming that the reference spots of the two transitions have exactly the same positions, Menten et al. (1992) found that another six of the strongest maser spots at 6.7 and 12 GHz have very good correspondence in positions and velocities. Figure 8 shows this association is a quite general phenomenon. Of the 27 maser spots at 6.7 GHz seen toward the 15 GHz continuum, 15 have 12 GHz counterparts. The distance between corresponding 6.7 and 12 GHz spots is always ≤ 3 mas, and the agreement in velocity is within 0.3 km s^{-1}, comparable with the velocity resolution (0.2 km s^{-1} at 6.7 GHz, 0.5 km s^{-1} at 12 GHz) of the data. The present data therefore support the conclusion that the two masers form in the same region but higher angular resolution observations at 6.7 GHz are needed to confirm this on spot size (a few mas) scale.

Higher angular resolution at 6.7 GHz would also allow measurements of the sizes and the brightness temperatures of the maser spots which could be compared with the values

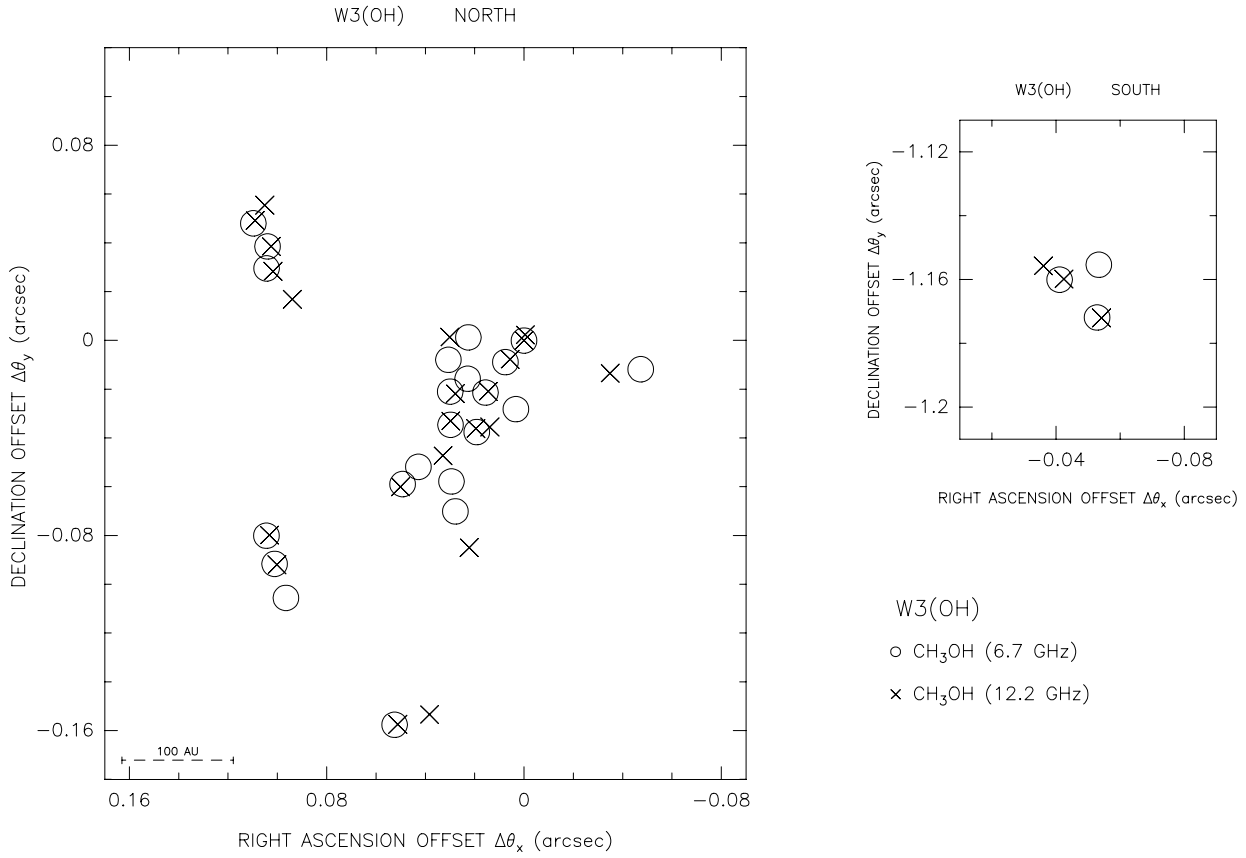

FIG. 8.—Comparison of the 1992 epoch 6.7 GHz and 1994 epoch 12 GHz CH_3OH maser observations. The open circles show the position of the 6.7 GHz CH_3OH spots measured by Menten et al. (1992), while the crosses show the components found in our observations after restoring the maps with the same beam as at 6.7 GHz (9.8 mas). The symbol size is equal to the FWHM of the beam. All positions are precessed to equinox J2000.0. The left-hand panel refers to the northern clump; the right-hand panel, to the southern one.

at 12 GHz. However for the 6.7 GHz reference spot, Menten et al. (1992) determined a size of 3 AU, which agrees well with that measured by us at 12 GHz, 4 AU. If one assumes that the areas of emission at 6.7 GHz and 12 GHz are the same, then the ratio of the flux densities gives also the ratio of the intensities and hence of the brightness temperatures. Furthermore, one can calculate the brightness temperature of a given spot of the low resolution 12 GHz map as the weighted[3] average of the brightness temperatures of the "real" spots into which it splits in the high-resolution map. In Figure 9, the ratio of 6.7 to 12 GHz brightnesses is plotted (in logarithmic scale) versus the brightness temperature at 12 GHz. Both the brightness ratio (from 1 to 300) and the 12 GHz brightness (from $\leq 10^{10}$ to 5×10^{11} K) extend over 2 orders of magnitude. The 6.7 to 12 GHz brightness ratios seem to be smaller (≤ 20) for the most intense 12 GHz spots ($\geq 10^{11}$ K), which is what one would expect if the 6.7 GHz brightness temperatures remained lower than a certain maximum value ($\approx 6 \times 10^{12}$ K), perhaps associated to the maximum amplification length. Comparing these measurements with the results of Sobolev et al. (1997), we note that the models have difficulty in obtaining 6.7 to 12 GHz intensity ratios above 5 and simultaneously maintaining 12 GHz brightness temperatures of the order 3×10^{10} K (corresponding to 6.7 GHz brightness of 1.5×10^{11} K) (see Fig. 2 of Sobolev et al. 1997).

As noted above, the 6.7 GHz maser spots toward W3(OH) are spread over a larger area than the 12 GHz ones. This is also observed toward other methanol maser sources. Of the six maser sources for which Norris et al. (1998) show both 12 and 6.7 GHz maps, five have a higher number of 6.7 GHz spots, distributed over a more extended area than the 12 GHz emission. Toward W3(OH), our analysis also shows that most of 12 GHz spots have a 6.7 GHz counterpart (see Fig. 8), whose brightness temperature is ≈ 10 times higher (see Fig. 9). The lower intensity of the 12 GHz masers, for physical and pumping conditions common with the 6.7 GHz masers, can explain the fact that they are observed distributed over smaller areas. Farther from the position of the most intense 12 and 6.7 GHz maser spots, the intensity of maser emission fades away, and potential 12 GHz counterparts of the weaker 6.7 GHz spots would not be detected.

In order to study the velocity profiles of the 12 GHz maser spots with the full spectral resolution available, 0.28 km s^{-1}, all the emission channels were mapped without applying postcorrelation Hanning smoothing. Then, at the peak position of each detected spot (averaging over an area of ≈ 1 AU of radius), the spectrum of the intensity was derived and Gaussians fitted for 46 spots of the 51 detected (counting also the double features). The FWHM of the

[3] The weight used is the emission area of the spot, given by the product of its major and minor axes.

TABLE 3

1994 (LOW-RESOLUTION[a]) AND 1988 SPOT PARAMETERS

1994 FEBRUARY OBSERVATIONS					1988 APRIL OBSERVATIONS				
Label	V_{LSR} (km s^{-1})	Flux (Jy)	$\Delta\alpha$ (mas)	$\Delta\delta$ (mas)	Label	V_{LSR} (km s^{-1})	Flux (Jy)	$\Delta\alpha$ (mas)	$\Delta\delta$ (mas)
A	−42.5	25	103.252(0.004)	−79.840(0.004)	1	−42.5	2.3	145.05(0.06)	−80.18(0.06)
B	−42.7	34	100.184(0.002)	−92.000(0.002)	2	−42.5	5.5	122.65(0.06)	−90.91(0.05)
C	−42.7	0.8	38.340(0.310)	−153.372(0.268)	3	−42.7	6.5	92.72(0.04)	−90.00(0.04)
D	−43.0	6.9	22.232(0.006)	−84.960(0.005)	4	−43.0	9.7	49.42(0.14)	−58.76(0.14)
Z	−43.0	115	−42.488(0.002)	−1159.832(0.002)	5	−43.0	3.5	72.51(0.16)	−155.80(0.16)
E	−43.0	8.3	50.092(0.038)	−60.024(0.038)	20.....	−43.0	17	−47.98(0.15)	−1157.30(0.15)
F	−43.0	25	51.216(0.002)	−157.424(0.002)	21.....	−43.0	36	−41.38(0.03)	−1159.70(0.02)
G	−43.2	15	32.912(0.004)	−47.252(0.003)	6	−43.4	9.3	7.31(0.20)	−37.30(0.36)
W.....	−43.4	54	−36.084(0.003)	−1155.704(0.006)	7	−43.6	19	13.15(1.15)	−36.18(0.58)
H	−43.6	100	13.828(0.004)	−35.528(0.004)	8	−43.6	24	10.79(0.36)	−39.73(0.39)
Y	−43.6	24	−54.224(0.002)	−1172.012(0.002)	9	−43.8	102	17.95(0.02)	−36.44(0.01)
K	−44.0	273	29.764(0.000)	−33.036(0.000)	10.....	−44.1	86	31.74(0.03)	−31.83(0.03)
J	−44.0	173	19.512(0.001)	−36.156(0.000)	11.....	−44.1	67	24.48(0.06)	−32.83(0.06)
I	−44.4	149	14.516(0.007)	−20.924(0.007)	12.....	−44.5	63	14.70(0.10)	−20.01(0.09)
L	−44.4	12	109.008(0.009)	49.168(0.009)	13.....	−44.5	25	−38.54(0.11)	−135.48(0.09)
M.....	−44.6	213	27.832(0.001)	−21.832(0.001)	14.....	−44.7	187	5.85(0.03)	−7.57(0.03)
N	−44.6	4.7	−34.880(0.043)	−13.452(0.050)	15.....	−44.7	137	28.25(0.01)	−20.32(0.01)
O	−44.8	11	105.100(0.008)	55.436(0.009)	16.....	−45.2	15	133.27(0.23)	99.25(0.24)
P	−44.8	9.2	30.112(0.057)	1.312(0.044)	17.....	−45.2	221	0.00	0.00
Q	−44.8	168	5.672(0.005)	−7.744(0.005)	18.....	−45.4	150	0.27(0.16)	3.76(0.25)
R	−45.1	341	0.000	0.000	19.....	−45.8	5.5	101.04(0.02)	28.62(0.02)
S.....	−45.1	7.1	93.908(0.018)	16.832(0.016)					
T	−45.5	196	−0.460(0.001)	2.300(0.001)					
U	−45.7	9.3	101.764(0.035)	28.328(0.035)					
V	−46.3	1.4	102.512(0.034)	38.572(0.037)					

[a] In the low-resolution maps, the restoring beam is circular with 9.8 mas FWHM.

spots is in the range 0.30–0.44 km s^{-1}, and thus, in many cases, lines are unresolved. However, 24 spots are marginally resolved with FWHM between 0.36 and 0.44 km s^{-1}, corresponding to intrinsic line widths up to 0.34 km s^{-1}.

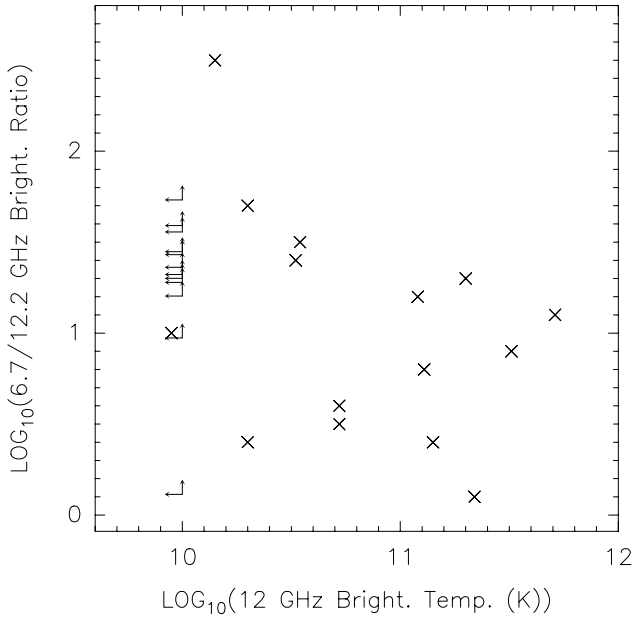

FIG. 9.—Ratio of the 6.7 to 12 GHz brightness temperatures is plotted vs. the 12 GHz brightness temperature. For both axes a logarithmic scale is used. The arrows give the upper-lower limits for the 6.7 GHz spots without 12 GHz counterparts. We use an upper limit for the undetected 12 GHz brightness temperatures of 10^{10} K, while the lower limits in the 6.7 to 12 GHz brightness ratios are derived assuming an upper limit for the undetected 12 GHz flux density of 10 Jy.

Is it reasonable to believe that the masers are saturated? In terms of the observed spot intensity, I, the saturation condition can be written as follows:

$$I > \frac{4\pi}{\Omega_m}\frac{\Gamma}{2B_{21}}, \quad (1)$$

where Ω_m is the solid angle of the maser beam, Γ is the decay rate from the maser levels, B_{21} is the Einstein coefficient for stimulated emission throughout the maser levels 1 (lower) and 2 (upper). For the 12 GHz CH_3OH $2_0 \rightarrow 3_{-1}$ E transition, $B_{21} = 3 \times 10^8$ cm^2 Hz sr ergs^{-1}. The decay rate Γ is of the same order as the collision rate, $\approx 10^{-10} n$ s^{-1} (Elitzur 1992), where n is the gas density in cm^{-3}. The region in which the 12 GHz methanol masers are found is the same as that of the 1665/1667 MHz OH masers: thermal line observations (NH_3; Guilloteau, Stier, & Downes 1983) of this region, and models for both the CH_3OH and OH maser transitions estimate $n \approx 3 \times 10^7$ cm^{-3} (Cesaroni & Walmsley 1991; Sobolev & Deguchi 1994). An educated guess concerning the beaming solid angle Ω_m suggests that it is in the range 10^{-4} to 10^{-1} sr, and hence the onset of saturated emission should occur somewhere between $T_b = 10^7$ and 10^{10} K. In general, the observed spots are brighter than this, and hence the assumption of saturated maser emission is reasonable.

5. COMPARISON WITH THE 1988 12.2 GHz OBSERVATIONS

The comparison of maser observations at different epochs allows one to investigate the cause of the variability of the emission. Concerning the variation of the position of maser spots, a basic question is whether it is caused by a real motion of blobs of gas ("proper motion") or rather by

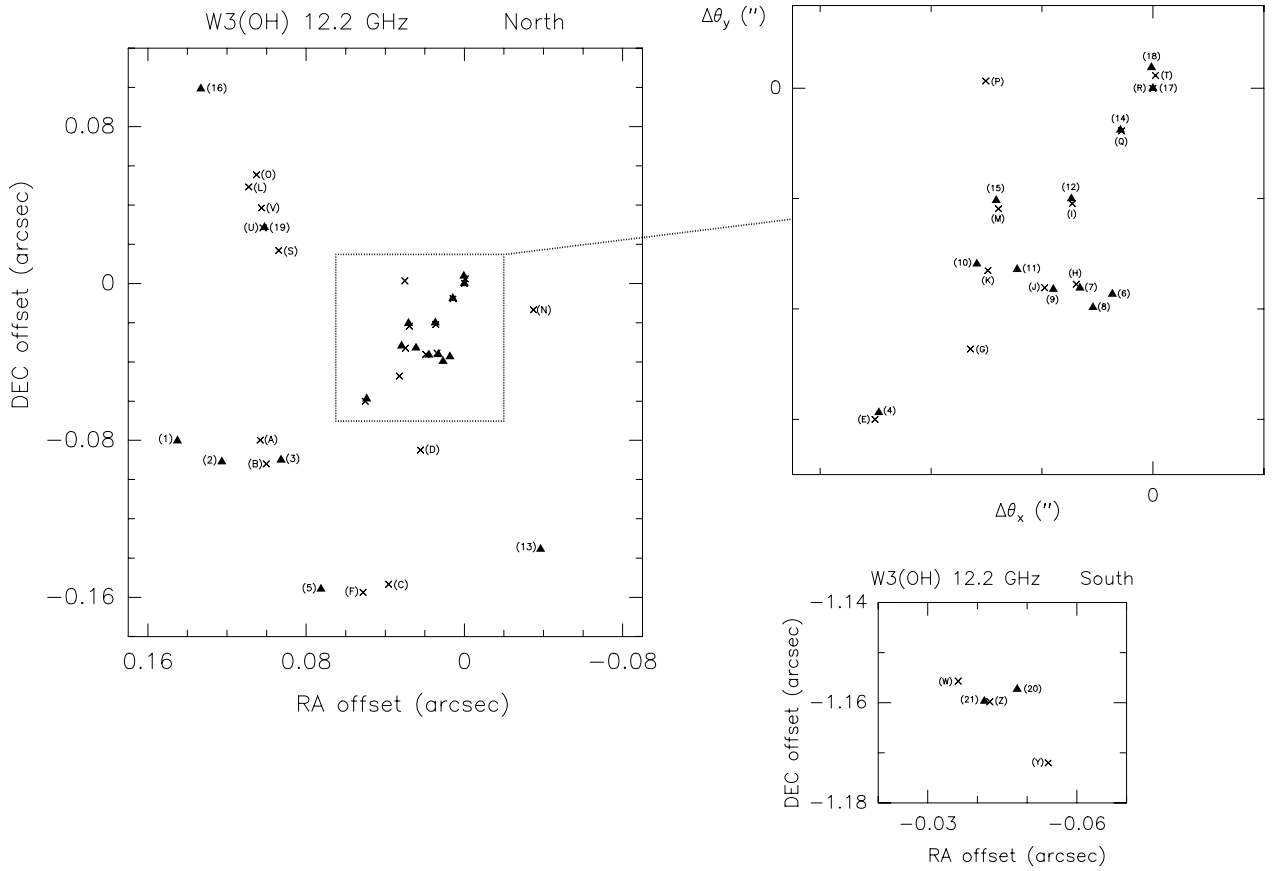

FIG. 10.—Comparison of the 1988 and 1994 epoch 12 GHz CH_3OH maser observations. The filled triangles show the position of the 12 GHz CH_3OH spots measured by Menten et al. (1988b), while the crosses individuate the components found in our observations after restoring the maps using the same beam as Menten et al. (1992) (9.8 mas). All the positions are precessed to equinox J2000.0. The 1988 epoch spots are labeled with numbers from 1 to 21, while the 1994 epoch spots with uppercase letters (see Table 3). The left-hand panel refers to the northern clump and the region inside the dotted line rectangle, corresponding to the same area plotted in Fig. 4, is shown in greater details in the upper right-hand panel of the figure. The lower right-hand panel compares the 1988 and 1994 epoch positions for the spots in the southern clump.

a change in the amplification paths ("Christmas tree effect"). An ordered motion of maser spots and/or persistency in the spot structures favors the proper-motion interpretation. If the proper motion of the maser spots is assumed to be of the same magnitude as the radial motion [taking for W3(OH) a conservative upper limit of 10 km s^{-1} for proper motion], one expects a maximum shift on the sky of 10 km $s^{-1} = 0.93$ mas yr^{-1} at the distance of W3(OH), thus implying 5.5 mas over the 5.86 yr between the 1988 and 1994 epochs.

In order to compare the spot positions, velocities, and fluxes of the 1988 observations with ours, our maps were restored using the same beam as Menten et al. (1988b) (9.8 mas), and the spot parameters were redetermined. Figure 10 compares the positions of the 1994 12.2 GHz spots with the positions of the 1988 12.2 GHz spots. The spot labels refer to Table 3, where the peak channel velocity, flux density, and positional offset with respect to the reference spots (labeled "R" and "17," respectively, for the 1994 and 1988 epochs) are listed. All the coordinates are precessed to equinox J2000.0.

In the case of the northern clump, over the 6 yr interval between the two VLBI observations, the general characteristics of the distribution of the emission are maintained. In 1988 as in 1994, the most intense maser spots are distributed in a short strip of about 80 mas in size (see Fig. 10, *inset*) which extends southeast from the most intense spot (the reference one). Along this line, as discussed above, there is a regular trend of radial velocities with position. Comparing the spot positions of the two epochs, while for the most intense spots (in the Fig. 10 inset), it is usually possible to find pairs of spots less than 5 mas apart, among the weaker spots, the only obvious pair is the one labeled (19,U). Since all the 1988 epoch spots for which a 1994 counterpart is not found are 5–10 times stronger than our sensitivity threshold, that implies a reduction of their flux density of at least 1 order of magnitude between the two epochs. Interestingly, these weaker, more variable spots are all located on the eastern and southern borders of the northern clump. As discussed in § 3, the relationship between radial velocities and angular separations for the 1994 epoch spots suggests that spots outside the inset of Figure 10 have different kinematics from those within.

The discussion above, based on Figure 10, assumes that the reference spot of the 1994 epoch coincides with that of the 1988 epoch. Thus, the position shifts between 1988 and 1994 seen on Figure 10 are relative to the reference spot. To convert these into proper motions thus requires an estimate

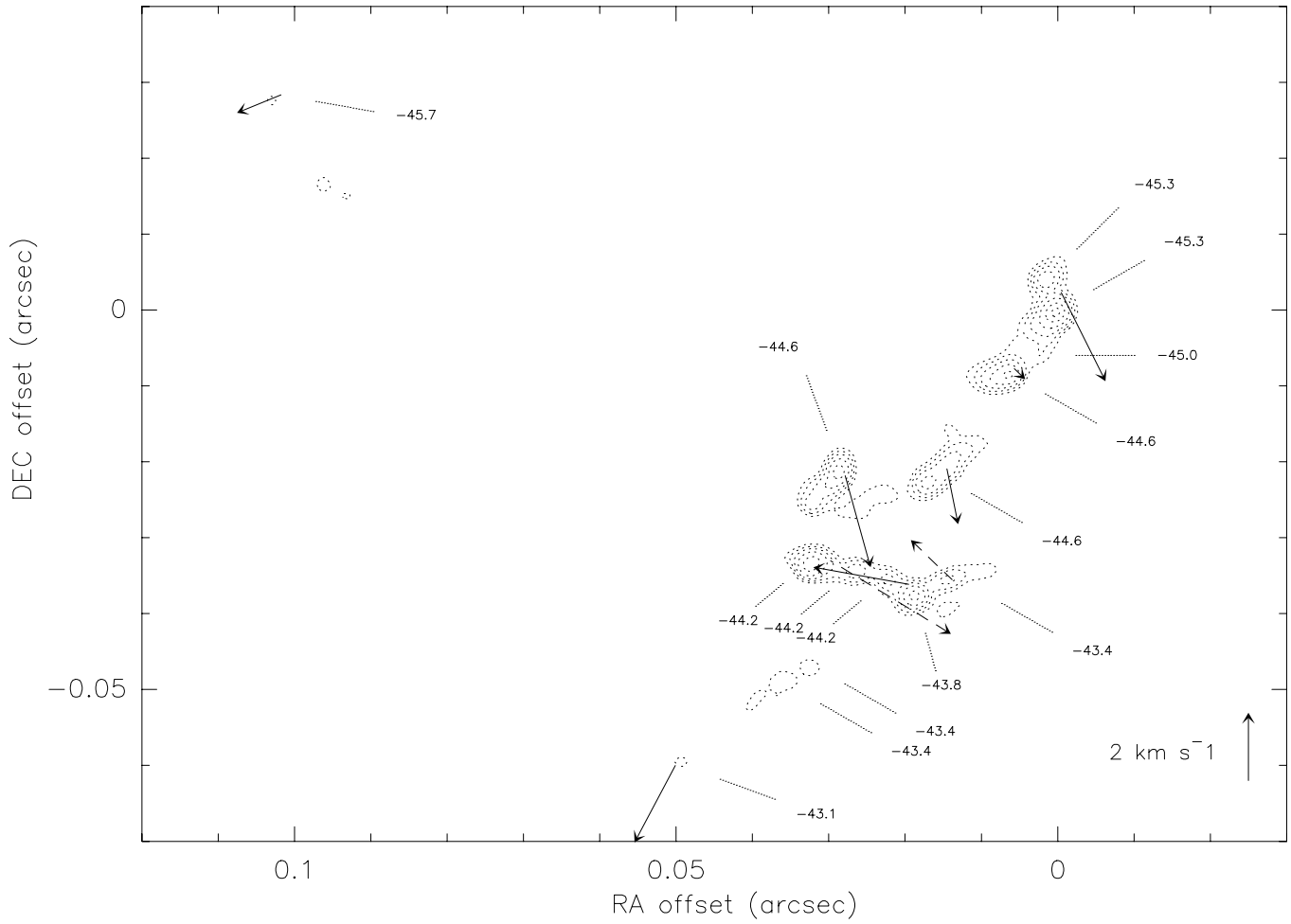

FIG. 11.—Vectors show the proper motions measured for the spots in the northern clump, with dashed-line vectors used in the case of bigger uncertainty, as explained in the text. The vector in the lower right-hand corner gives the velocity scale. The proper motions are superimposed on the (*dotted line*) contour plot of the emission averaged over velocity channels between −42.7 and −46.1 km s^{-1}. The dotted line pointers indicate the position of the main features of the different velocity channels. The levels of brightness temperature used in the contour plot are 0.2, 0.4, 0.75, 1.5, 3.0, 4.5 × 10^{10} K.

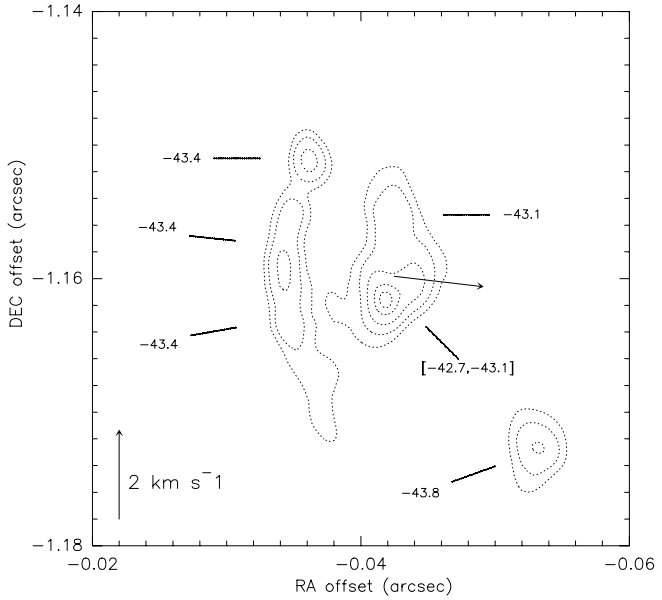

FIG. 12.—Vector at the center of the figure shows the single proper motion measured in the southern clump. The velocity scale is given in the lower left-hand corner. The (*dotted line*) contour plot of the emission averaged over velocity channels between −42.7 and −43.8 km s^{-1} is also shown. The dotted line pointers indicate the position of the main features of the different velocity channels. The levels of brightness temperature used in the contour plot are 2.6, 5.1, 10, 18, 23 × 10^9 K.

of the proper motion of the reference spot, which we presently do not have. However, we have checked the number of spot pairs found for a grid of proper motions of the reference spot, assuming that the number of pairs will be maximized for the true reference spot proper motion. From this study, we conclude that the reference spot has moved less than 5 mas and thus that our assumption of spot velocities less than 10 km s^{-1} is correct.

Figures 11 and 12, for the northern and southern clumps, respectively, show the relative proper motions overlaid on the contour plots of the integrated maser emission, averaged over the velocity channels with emission. These have considerable uncertainty for a number of reasons. The principal reason is the fact that essentially all of the "spots" show structure on the scale of a few mas, and this leads to errors in the inferred proper motions as well as in the identification of "spot pairs" at two different epochs. Thus, the proper-motion vectors shown in Figures 11 and 12 should be considered as "tentative." In cases in which the uncertainty is judged to be particularly large, the vectors are shown to be dashed. Bearing this in mind, we note that several of the vectors in Figure 11 are at large angles to the linear structure discussed earlier.

We think it is likely that the strip of intense maser spots of the northern clump along the axis shown in Figure 4 (see also Fig. 10, *inset*) are tracing an ordered pattern of motion. The gradient of radial velocity that we have estimated along this axis is similar to that found by Minier, Booth, & Conway (1998) for a smaller "line of masers" associated with NGC 7538, which they believe is associated with a Keplerian disk surrounding a massive star seen edge-on. In the case of W3(OH), there is presently no clear evidence for this. Observations at another epoch with the VLBA as well as measurements of the reference spot proper motion are clearly needed.

6. CONCLUSIONS

Our observations have determined for the first time the sizes of the 12 GHz CH_3OH maser spots toward W3(OH) and have allowed a better estimation of their brightness temperatures. The linear sizes range from ≤ 2 to 10 AU, and the brightness temperatures extend over the interval 10^9 to 6×10^{11} K. The brightness temperatures may be higher than the measured values (by a factor ≤ 10) owing to the fact that most of the spectral profiles of the maser spots are unresolved with our velocity resolution. Comparing our observations with those at 6.7 GHz of Menten et al. (1992), more than half of the 6.7 GHz spots are found to have a 12 GHz counterpart at the same position (within a few mas) and velocity (within 0.3 km s^{-1}). It seems likely therefore that both transitions are tracing the same physical entities. Our data suggest also the presence of a spatially extended component of maser emission whose size might be comparable to that of the spot clumps, 50–100 mas, and with brightness temperature less than few 10^9 K.

We have compared our 1994 VLBA observations with the three-station VLBI experiment of Menten et al. (1988b) to study the variability of the 12 GHz maser emission toward W3(OH). For the most intense spots of the northern clump, distributed along an axis at P.A. = 141°, proper motions relative to a reference spot of a few km s^{-1} in magnitude are derived. The same group of spots shows a regular trend of radial velocities with position, and, therefore, there is evidence that they are tracing some structure with a well-defined pattern of motion.

REFERENCES

Bloemhof, E. E., Reid, M. J., & Moran, J. M. 1992, ApJ, 397, 500
Campbell, M. F., Lester, D. F., Harvey, P. M., & Joy, M. 1989, ApJ, 345, 298
Cesaroni, R., & Walmsley, C. M. 1991, A&A, 241, 537
Dreher, J. W., & Welch, W. J. 1981, ApJ, 245, 857
Elitzur, M., ed. 1992, Astronomical Masers (Dordrecht: Kluwer)
Guilloteau, S., Stier, M. T., & Downes, D. 1983, A&A, 126, 10
Humphreys, R. M. 1978, ApJS, 38, 309
Kawamura, J. H., & Masson, C. R. 1998, ApJ, 509, 270
Menten, K. M., Johnston, K. J., Wadiak, E. J., Walmsley, C. M., & Wilson, T. L. 1988a, ApJ, 331, L41
Menten, K. M., Reid, M. J., Moran, J. M., Wilson, T. L., Johnston K. J., & Batrla, W. 1988b, ApJ, 333, L83
Menten, K. M., Reid, M. J., Pratap, P., Moran, J. M., & Wilson, T. L. 1992, ApJ, 401, L39
Minier, V., Booth, R. S., & Conway, J. E. 1998, A&A, 336, L5
Norris, R. P., et al. 1998, ApJ, 508, 275
Norris, R. P., McCutcheon, W. H., Caswell, J. L., Wellington, K. J., Reynolds, J. E., Peng, R. S., & Kesteven, M. J. 1988, Nature, 335, 149
Norris, R. P., Whiteoak J. B., Caswell, J. L., Wieringa, M. H., & Gough, R. G. 1993, ApJ, 412, 222
Reid, M. J., Haschick, A., Burke, B. F., Moran, J. M., Johnston, K. J., & Swenson, G. W., Jr. 1980, ApJ, 239, 89
Scott, P. F. 1981, MNRAS, 194, 25
Sobolev, A. M., Cragg, D. M., & Godfrey, P. D. 1997, A&A, 324, 211
Sobolev, A. M., & Deguchi, S. 1994, A&A, 291, 569
Wilner, D. J., Reid, M. J., & Menten, K. M. 1999, ApJ, 513, 775